Journal of Materials Chemistry A

Accepted Manuscript

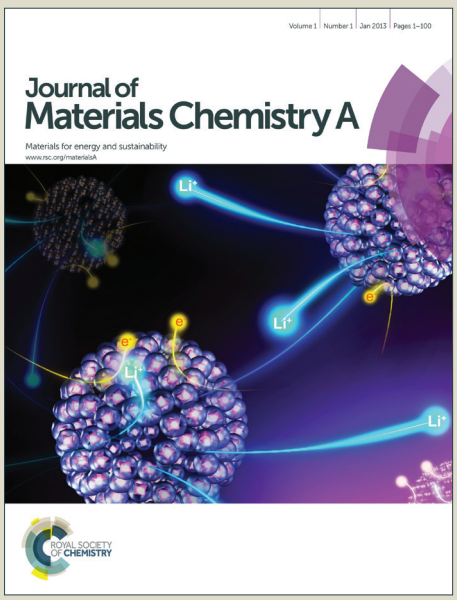

ROYAL SOCIETY OF CHEMISTRY

www.rsc.org/materialsA

Cite this: DOI: 10.1039/c0xx00000x

www.rsc.org/xxxxxx

ARTICLE TYPE

One-Pot Synthesis of $CoFe_2O_4$/Graphene Oxide Hybrids and Their Conversion into FeCo/Graphene Hybrids for Lightweight and High Efficient Microwave Absorber

Xinghua Li[§a,b], Juan Feng[§b], Yaping Du[c], Jintao Bai[a], Haiming Fan*[a,d], Haoli Zhang[e], Yong Peng*[b], Fashen Li[b]

Received (in XXX, XXX) Xth XXXXXXXXX 20XX, Accepted Xth XXXXXXXXX 20XX
DOI: 10.1039/b000000x

$CoFe_2O_4$/graphene oxide hybrids have been successfully fabricated via a facile one-pot polyol route, followed by chemical conversion into FeCo/graphene hybrids under H_2/NH_3 atomosphere. These magnetic nanocrystals uniformly decorated on the entire graphene nanosheets without aggregation. The morphology, chemical composition and crystal structure have been characterized in detail. In particular, FeCo/graphene hybrids show significant improvement in both permeability and permittivity due to the combination of high magnetocrystalline anisotropy of metallic FeCo and high conductivity of light-weight graphene. This leads to remarkable enhancement in microwave absorption properties. The maximum reflection loss of FeCo/graphene hybrids reaches -40.2 dB at 8.9 GHz with a matching thickness of only 2.5 mm, and the absorption bandwidth with reflection loss exceeding -10 dB is in 3.4-18 GHz range for the absorber thickness of only 1.5-5 mm. Moreover, the experimental relationship between matching thickness and frequency is found to obey the quarter-wavelength matching model, facilitating the design of FeCo/graphene hybrids film for practical application. The results suggest that the FeCo/graphene hybrids developed here can serve as ideal candidate for the manufacture of light-weight and high-efficiency microwave-absorbing devices.

Introduction

With the rapid development of telecommunications, microwave darkrooms and digital systems, much attention has been focused on the exploration of microwave absorbers, not only for their great potential in civilian applications including the reduction of electromagnetic radiation (EMR) and the improvement of electromagnetic compatibility (EMC) among wireless communications and circuit devices, but also for the military purpose such as radar invisible aircraft, tanks and targets.[1-4] The center issue in this field is the fabrication of ideal and high-efficiency microwave absorbing materials that possess strong adsorption characteristics, broad band adsorption, light weight and thin matching thickness.[5] Since complex permeability ($\mu_r = \mu' - j\mu''$) and permittivity ($\varepsilon_r = \varepsilon' - j\varepsilon''$) of the microwave absorbers play key roles in determining their microwave absorption properties, two types of microwave absorbing materials have been widely investigated: (1) magnetic loss materials such as ferrite,[6] Fe,[7] Co,[8] Ni[9] and so on, (2) dielectric loss materials like SiC,[10] $BaTiO_3$,[11] MnO_2,[12] CuS[13] and carbon-based materials.[14-16] However, it is quite difficult for these unilateral magnetic loss or dielectric loss materials to achieve impedance match condition ($Z_m=Z_0(\mu_r/\varepsilon_r)^{1/2}$).[17] To gain excellent microwave absorption properties, much effort has been devoted to the fabrication of composites or hybrids in which magnetic loss materials were elaborately combined with dielectric loss materials. Examples including Fe_3O_4@TiO_2,[1,5] Fe@SiO_2,[18] Fe_3O_4/basalt fibers,[19] Ni/polyaniline,[20] Fe/ZnO[21] and Fe_3Al/Al_2O_3.[22] Nevetheless, the high density and large matching thickness of these magneto/dielectric absorption materials greatly restrict their practical applications. The demand for the development of high-efficiency microwave absorption materials with light weight and thin matching thickness is urgently required.

According to the quarter-wavelength matching model,[23] the enhanced complex permeability (μ_r) and permittivity (ε_r) are necessary for the composite absorbers with a thin matching thickness. Since further improvement of the efficiency of currently reported absorbers by varying magnetic components and the permeability is quite limited, much attention has been directed to seek innovative dielectric materials with light weight and unique electrical properties. Carbon as light weight, low cost and high electrical conductivity materials thus attracts significant interest. So far, various carbon materials like graphite, Buckminster fullerene and nanotube have been used to construct composite materials for microwave absorption applications such as Ni/C, CoNi/C, FeNi/C, FeCu/C, FeCo/CNTs, Fe/Co/Ni/CNTs, Fe/CNTs, FeNi/CNTs and Fe_3O_4/MWCNTs.[17,24-33] In particular, Graphene, a two-dimensional single layer of sp^2-hybridized carbon,[34] are the promising candidate for constructing composite absorber because of its exceptional physical properties including

high intrinsic mobility, excellent thermal conductivity, strong mechanical stiffness, high Young's modulus, optical transmittance and large specific surface area.[35-43] For instance, its large surface facilitates high loading of magnetic particle components, while superior electrical and thermal conductivity promote the conversion of incident electromagnetic wave into thermal energy.[44,45] These merits have been demonstrated by graphene/polymer hybrids that exhibited significantly improved microwave absorption.[16,46-48] However, the intrinsic poor impedance match condition in such graphene/polymer system hinders further improvement of application performance. Decorating graphene with inorganic magnetic nanoparticles is a popular way to construct innovative hybrid materials with superior properties for improved application performance. By the combination of inorganic nanocrystals and graphene, such system could possess rich chemical/physical properties as well as synergistic effect, if any.[49-54] Magnetic nanoparticle-graphene hybrid materials as light-weight microwave absorption materials have also been reported.[23,63-71] Despite that these hybrid materials have shown enhanced microwave-absorbing, the complex synthetic process during the fabrication may hinder their industrial applications. Moreover, the magnetic nanoparticles grown on the graphene nanosheets are usually aggregated in reported magnetic nanoparticle/graphene hybrid systems,[64,68,72-74] leading to uneven distribution and possible "dead area" with null magnetic components. Therefore, the development of a facile synthesis that ensure magnetic nanoparticles uniformly decorated on the whole graphene nanosheets without aggregation is urgently needed.[73-76] In addition, the magnetic component employed in above studies are usually Fe_3O_4, Co_3O_4, Fe_2O_3, $NiFe_2O_4$ with relative low saturation magnetization. By contrast, metallic FeCo alloys possessing the large saturation magnetization, high curie temperature and high conductivity, is more desirable for constructing high performance magnetic nanoparticle/graphene hybrid microwave absorber.[77,78] To our best knowledge, investigations on the fabrication and microwave absorption properties of light-weighted FeCo/graphene hybrids has yet to report to date.

In the present study, we successfully prepared light-weight sandwich-structured $CoFe_2O_4$/graphene oxide hybrids by a facile one-pot polyol method, followed by chemical converting into FeCo/graphene hybrid materials to pursue the high performance microwave absorption properties. The obtained hybrids show FeCo/graphene/FeCo sandwich-like structure, in which FeCo nanoparticle with size of ~100 nm are evenly distributed on the graphene forming a single layer. At the same time, no freestanding or aggregated FeCo nanoparticles are produced, indicating validity of this synthetic process. Microwave absorption measurements revealed that the FeCo/graphene hybrids perform a minimum reflection loss (RL) value of -40.2 dB at 8.9 GHz with a matching thickness of only 2.5 mm, 2.5 times larger than $CoFe_2O_4$/graphene oxide hybrids. This is also the largest RL value among the reported magnetic nanoparticles-graphene hybrid systems with a thickness within 3 mm.[23, 63-71] Furthermore, it also exhibits a broad bandwidth (RL ≤ -10 dB) in 3.4-18 GHz range for the thicknesses of 1.5-6.0 mm. These enhanced microwave-absorbing behaviors for both $CoFe_2O_4$/graphene oxide and FeCo/graphene hybrids could be well explained by the quarter-wavelength matching model. This study aims to develop a facile approach to fabricate high-performance magnetic nanocrystals/graphene hybrids microwave absorber as well as investigate synergistic interaction between the magnetic nanocrystals and graphene for practical applications in the future.

Experimental Section

Materials

All chemical reagents were of analytical grade and used without further purification in this work. Natural graphite flake powder was bought from Beijing Creative Biological Engineering Materials Co. Ltd. Trimethylene glycol (TEG), ferric chloride hexahydrate ($FeCl_3 \cdot 6H_2O$) and cobalt (Ⅱ) chloride hexahydrate ($CoCl_2 \cdot 6H_2O$) were purchased from Tianjin Guangfu Fine Chemical Research Institute. Sodium acetate ($NaCOOCH_3$, NaAc) was bought from Sichuan Xilong Chemical Company.

Synthesis of graphene oxide (GO)

Graphene oxide (GO) was fabricated from natural flake graphite powder through a modified Hummers method. In a typical process, 5 g of P_2O_5 and 5 g of $K_2S_2O_8$ were dissolved in 30 ml of H_2SO_4 (98 %) at 90 ^oC, and then the mixture was maintained at 80 ^oC. 0.15 g of natural graphite flake was carefully added to the above solution at 80 ^oC and stirred for 4.5 h. Then the solution was cooled down to room temperature and diluted with deionized water. The mixture was filtered by Nylon film (0.2 micron) and washed by deionized water until the filtrate was neutral. The pretreated graphite powders and 1.5 g of $KMnO_4$ were slowly added to 12 ml of H_2SO_4 (98 %) at 0 ^oC. Successively, the mixture was slowly increased to 35 ^oC and stirred for 2 h. 25 ml of deionized water was added to the mixture, followed by heating to reflux at 90 ^oC for another 0.5 h. The solution was cold down to room temperature and diluted by deionized water (75 ml). H_2O_2 (30 %) was dropped to the solution until the color became brilliant yellow. Then the solution was washed by performing dialysis to remove the residual ion. Finally, the yellow solution was subjected to centrifugation at 12,000 rpm for 20 min, and GO was obtained.

Synthesis of $CoFe_2O_4$/GO hybrids

$CoFe_2O_4$/GO hybrids were synthesized by an one-pot polyol method. Typically, GO (40 mg) was dissolved into TEG (100 ml) and then ultrasounded for 3 h to produce GO with few layers. $FeCl_3 \cdot 6H_2O$ (4 mmol) and $CoCl_2 \cdot 6H_2O$ (2 mmol) were dispersed into the above GO-containing solution and treated by ultrasound for additional 3 h. Then, NaAc (30 mmol, with a molar ratio of Ac^- : M^{n+} = 5:1) was dissolved in the above solution. Finally, the solution was heated to reflux for 20 h with strong stirring. The obtained products were centrifugated at 10,000 rpm and washed by water and ethanol for several times.

Synthesis of FeCo/graphene (FeCo/GNs) hybrids

FeCo/graphene hybrids were fabricated by H_2/NH_3-thermal reduction method. Sandwich-structured $CoFe_2O_4$/GO hybrids were reduced in H_2/NH_3 (10:90) atmosphere at 550 ^oC for 2 h, and FeCo/GNs hybrids were obtained. In this process, GO was reduced into graphene nanosheets (GNs) accompanied with the

formation of FeCo alloy nanocrystals. The obtained products were cooled down to room temperature naturally under N_2 atomosphere in the furnace.

Characterization

The morphology and microstructure of the products were characterized using field-emission scanning electron microscopy (SEM, Hitachi S-4800, Japan) and high-resolution transmission electron microscope (HRTEM, FEI Tecnal G^2 F30) embedded with energy-dispersive X-Ray spectroscopy (EDX, Oxford Instrument), high angle annular dark field (HAADF), and scanning transmission electron microscopy (STEM). The crystal phase were carried out by X-ray diffraction instrument with Cu K_α radiation (λ=1.5418 Å) (XRD, X'pert powder, Philips). Fourier transform infrared spectroscopy (FTIR) of the products was analyzed by a 170SX spectrometer in the range of 400-4000 cm^{-1}. Raman spectra were performed on an in Via Reinishaw confocal spectrometer with 633 nm laser. The magnetic properties of the products were studied by vibrating sample magnetometer (VSM, Lake Shore 7,304).

Electromagnetic measurements

The microwave absorption properties of the $CoFe_2O_4$/GO and FeCo/GNs hybrids were investigated through a network analyzer (Agilent Technologies E8363B) in the frequency range of 0.1-18 GHz. The composites for microwave absorption measurement were fabricated by mixing paraffin with 50 wt% hybrids and pressed into toroidal shape (ψ_{out}: 7.00 mm, ψ_{in}: 3.04 mm). The complex permeability and permittivity were computed from the experimental scattering parameters through the standard Nicholson-Rossand Weir theoretical calculations.[79]

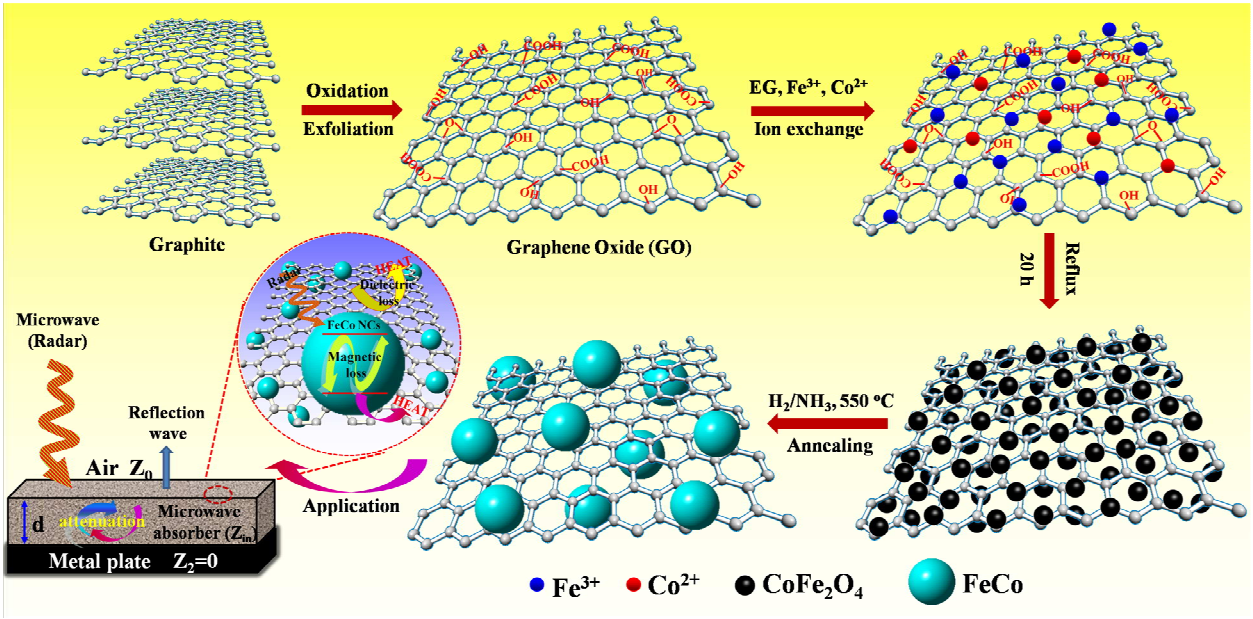

Fig. 1 Schematic illustration of $CoFe_2O_4$/GO and FeCo/GNs hybrids formation and their application for microwave absorption

Results and Discussion

The formation process of $CoFe_2O_4$/GO and FeCo/GNs hybrids in this work is schematically illustrated in Fig. 1. Sandwich-structured $CoFe_2O_4$/GO hybrids were synthesized by thermal decomposition of metal salt in the presence of GO through a facile one-pot polyol route, in which NaAc acts as a stabilizer and TEG was used as the solvent. In order to obtain the uniform distribution of magnetic nanocrystals and against potential aggregation during growth process, metal ions were firstly anchored and coordinated onto the oxygen-based functional groups on the surface of GO nanosheets via ultrasonication approach. Then, the reaction temperature was increased to 160 °C and reflux for 20 hours. During this period, $CoFe_2O_4$ nanocrystals were in-situ nucleated and grown on both sides of nanosheets, leading to the sandwich-structured $CoFe_2O_4$/GO hybrids. $CoFe_2O_4$ nanocrystals are tightly anchored on the GO nanosheets directly and no additional linkers are needed to bridge them. In addition, the $CoFe_2O_4$/GO hybrids show high stability against sonication, suggesting a strong covalent interaction between the $CoFe_2O_4$ nanocrystals and GO nanosheets. FeCo/GNs hybrids were obtained by reduction treatment of $CoFe_2O_4$/GO hybrids in H_2/NH_3 (10:90) atmosphere at 550 °C. During the annealing process, the GO was transformed into GNs while $CoFe_2O_4$ was converted into FeCo alloy nanocrystals.

The phase structures of natural graphite, graphene oxide (GO), $CoFe_2O_4$/GO and FeCo/GNs hybrids were measured by XRD, as displayed in Fig. 2. The original graphite (Fig. 2 (a)) shows a sharp diffraction peak at 26.5 °, corresponding to its (002) crystal plane with an interplanar spacing of 0.34 nm. As for the GO, a broad diffraction peak at 13.4 ° is observed instead of the sharp peak for graphite, indicating the introduction of oxygen-based functional groups on the surface of the graphite nanosheets.[67,68] Noted that similar peak is also observed for graphite oxides, the appearance of this peak in our case may be due to the strong interaction between the sheets and aggregation of GO during the drying process. For the $CoFe_2O_4$/GO hybrids (Fig. 2 (c)), the positions and relative intensities of all the diffraction peaks are in consistent with the standard XRD pattern for cubic spinel structure of bulk $CoFe_2O_4$ (JCPDS No. 22-1086). The broadening diffraction peaks is due to the small size effect of $CoFe_2O_4$ nanocrystals. Based on the Scherer's formula, the

average grain size of the $CoFe_2O_4$ nanocrystals is about 4.7 nm. After H_2/NH_3 annealing treatment, the XRD pattern of the product (Fig. 2 (d)) shows the peaks at 44.5, 65.1 and 82.4 °, which can be indexed to (111), (200) and (211) crystal planes of body-centered cubic (bcc) FeCo alloy (JCPDS No. 48-1816), indicating the phase transformation from $CoFe_2O_4$ ferrite to FeCo alloy. At the same time, GO was reduced to GNs. The estimated grain size of the FeCo nanocrystals is about 40 nm that is significantly larger than original $CoFe_2O_4$ nanocrystals. In addition, the characteristic peak shown in GO powder are not observed in the $CoFe_2O_4$/GO and FeCo/GNs hybrids, confirming that GO powder were dispersed into separated GO again in solution under ultrasonation. Energy-dispersive X-Ray (EDX) spectra of the $CoFe_2O_4$/GO and FeCo/GNs hybrids are presented in Fig. S1. The spectra show that the atomic ratio of Co and Fe are around 0.48 and 0.94 in $CoFe_2O_4$/GO and FeCo/GNs hybrids, respectively, which is consistent with the XRD results. The additional Cu and Si peaks resulted from the copper grids which were confirmed by the EDX data of an empty copper grid.

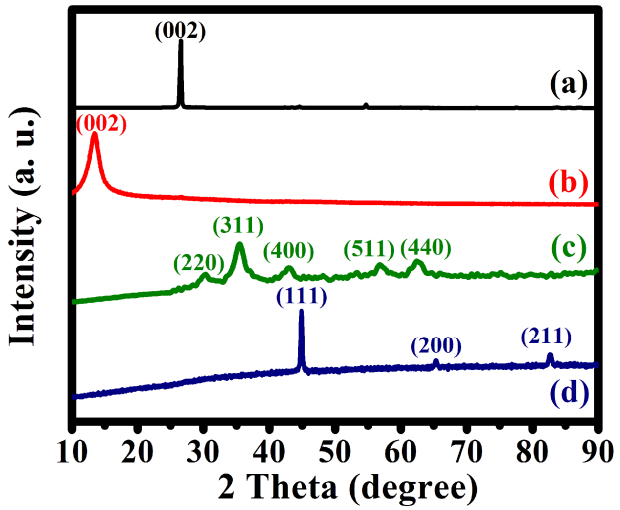

Fig. 2 XRD patterns of (a) graphite, (b) GO, (c) $CoFe_2O_4$/GO and (d) FeCo/GNs hybrids.

The morphologies and microstructures of GO, $CoFe_2O_4$/GO and FeCo/GNs hybrids were further characterized by using scanning electron microscopy (SEM) and transmission electron microscopy (TEM). Fig. 3 displays the SEM images of GO powder, $CoFe_2O_4$/GO hybrids and FeCo/GNs hybrids. As shown in Fig. 3 (a), the aggregated GO powder shows a crumpled flaky structure with average thickness of 200-600 nm, which is in consist to our XRD observation. After in situ growth, $CoFe_2O_4$ nanocrystals were uniformly decorated on both sides of GO, forming sandwich-structured $CoFe_2O_4$/GO hybrids (Fig. 3 (b)). The particle size cannot be well resolved under SEM due to small size of $CoFe_2O_4$. The converting of $CoFe_2O_4$ to FeCo promotes the growth of grain size and simultaneously decreases the particle density on the GO as shown in Fig. 3 (c). Though large FeCo nanocrystals with irregular shapes and sizes of 40-150 nm were found, the sandwich-structure is perfectly retained. The representative TEM images of GO, $CoFe_2O_4$/GO and FeCo/GNs hybrids are shown in Fig. 4. After re-disperse into ethanol solution, the GO was transferred into copper grid for TEM measurement. In this case, the thin and wrinkled GO nanosheet (Fig. 4 (a, d)) appears and is almost transparent under TEM observation. The high resolution TEM (HRTEM) image of GO (inset of Fig. 4 (d)) suggests that each GO flake is comprised of

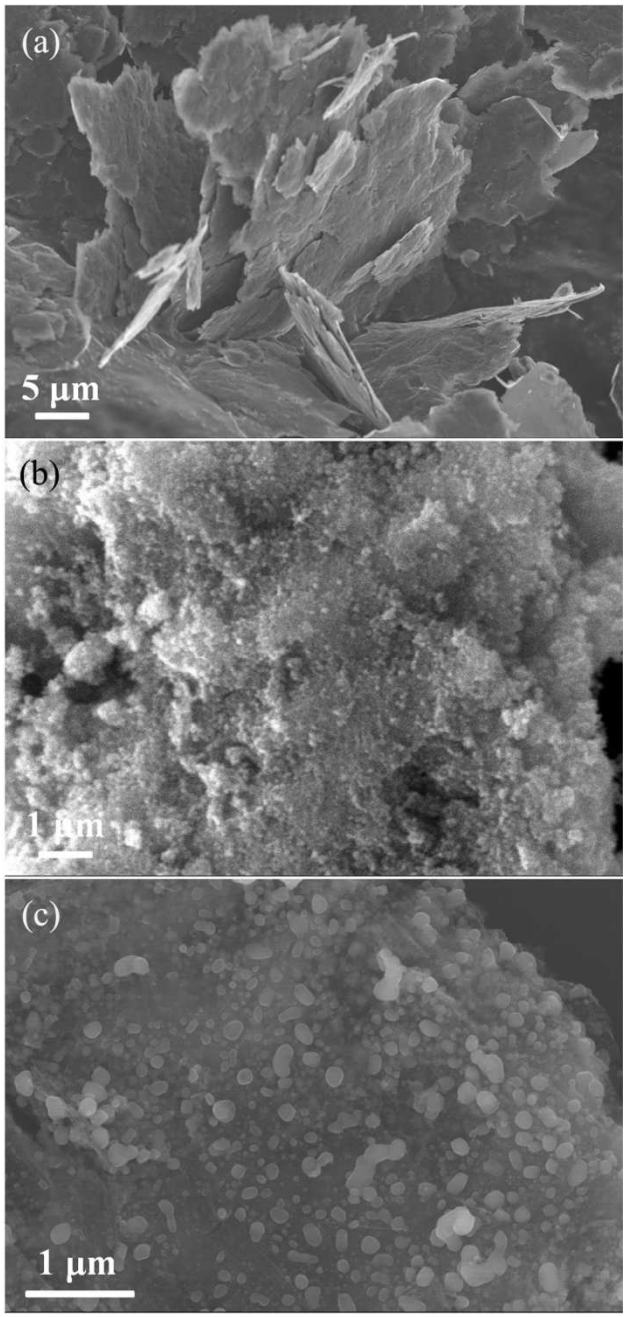

Fig. 3 SEM images of (a) GO, (b) $CoFe_2O_4$/GO and (c) FeCo/GNs hybrids.

about 3 graphene layers. This is in consistent with the AFM analysis where the estimated height of GO is 1.5 nm, 2-3 times of the interlayer spacing of GO (0.67 nm) (Fig. S2). The selected area electron diffraction (SAED) pattern of GO is presented in Fig. 4 (g). The well-defined diffraction spots for GO indicate the high crystalline nature with a hexagonal closed-packed (hcp) structure. A set of six fold patterns in the reciprocal space show a weak and monotonous intensity, suggesting that the initial GO is few-layer.[80] Fig. 4 (d) and (e) show a sandwich-like structured $CoFe_2O_4$/GO hybrids. The whole graphene sheets are

homogeneously covered by tiny $CoFe_2O_4$ nanocrystals with sizes of about 5 nm. It is worth noting that no freestanding nanoparticle is observed out of graphene sheet, implying in situ nucleation and growth of $CoFe_2O_4$ nanocrystals. The interplanar spacing for the $CoFe_2O_4$ nanocrystals (inset of Fig. 4 (e)) is about 0.254 nm, which corresponds to (311) plane of $CoFe_2O_4$. SAED pattern of the $CoFe_2O_4$/GO hybrids (Fig. 4 (h)) shows a face-centered cubic (fcc) structure, which is in accordance with the diffraction patterns of $CoFe_2O_4$. For the FeCo/GNs hybrids (Fig. 4 (c, f)), irregular-shaped FeCo nanocrystals with a size of 40-150 nm are clearly observed, similar to the SEM observation. Surprisingly, these nanocrystals still firmly anchored on the surface of graphene after thermal treatment and no crystals is found out of the graphene. Moreover, the nanocrystals are separated each other without any aggregation. The lattice distance of FeCo nanocrystals in FeCo/GNs hybrids (inset of Fig. 4 (f)) is measured to be 0.200 nm and is indexed to the (110) crystallographic plane of FeCo alloys, showing its single-crystalline nature. The SAED of FeCo nanocrystals shows the bright diffraction rings, indicating the body-centered cubic (bcc) structure of FeCo alloy. These results reveal that the synthetic method developed in this work could effectively prepare high-quality FeCo/GN hybrid structures with well-dispersed FeCo nanocrystals on graphene.

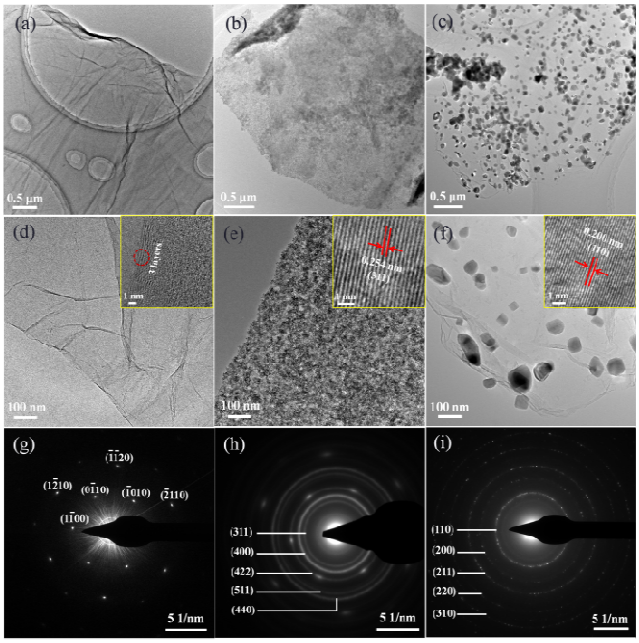

Fig. 4 Representative TEM images of (a, d) GO, (b, e) $CoFe_2O_4$/GO and (c, f) FeCo/GNs hybrids at different magnifications. Insets show the HRTEM images of GO, $CoFe_2O_4$/GO and FeCo/GNs in d, e and f, respectively; SAED patterns of (g) GO, (h) $CoFe_2O_4$/GO and (i) FeCo/GNs.

The structural changes and chemical bonding of carbonaceous materials were characterized by Raman and FT-IR spectroscopy techniques. Fig. 5 shows the Raman spectra of GO, $CoFe_2O_4$/GO and FeCo/GNs hybrids. The Raman spectra show two characteristic peaks, corresponding to the D band at ~ 1340 cm^{-1} and G band at ~ 1590 cm^{-1}. The G band is attributed to the E_{2g}-vibration mode, while the D band is associated with the A_{1g} mode of the small crystallites, or boundaries of larger crystallites.[57] The intensity ratio of D band to G band (D/G) is adopted to investigate the disordered structure of carbon-based materials. The D/G intensity ratios are 0.75 for GO, 0.99 for

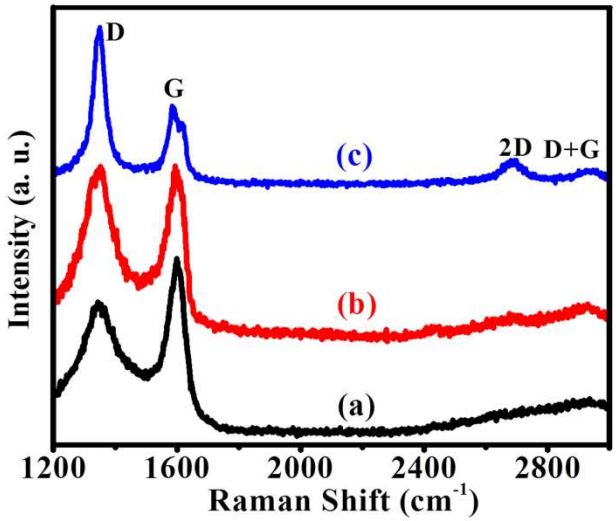

Fig. 5 Raman spectra of (a) GO, (b) $CoFe_2O_4$/GO and (c) FeCo/GNs hybrids.

$CoFe_2O_4$/GO and 2.08 for FeCo/GNs hybrids, respectively. The obvious enhancement of I_D/I_G as well as the appearance of 2D band at 2678 cm^{-1} for FeCo/GNs hybrids indicates the formation of more small sized aromatic domains, suggesting that GO was reduced to graphene in FeCo/GNs hybrids.[63,64] In addition, the increased C-C sp^2 bond of the graphene may be beneficial for improvement of the conductivity of graphene.[81]

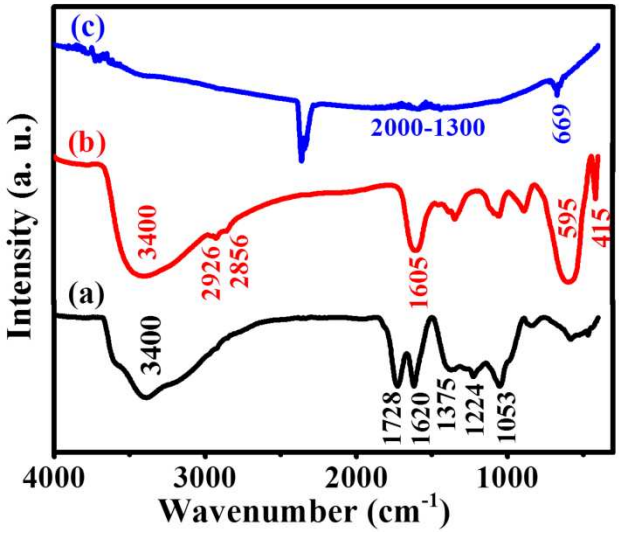

Fig. 6 FTIR spectra of (a) GO, (b) $CoFe_2O_4$/GO and (c) FeCo/GNs hybrids.

Figure 6 shows the FTIR spectra of GO, $CoFe_2O_4$/GO and FeCo/GNs hybrids. The characteristic peaks for GO confirm the existence of oxygen-containing functional groups on the surface of nanosheets, including O-H (3400 cm^{-1}), C=O (1728 cm^{-1}), carboxy C-O (1375 cm^{-1}), epoxy C-O (1224 cm^{-1}) and C-O (1053 cm^{-1}). The peak at 1620 cm^{-1} is assigned to the aromatic C=C stretching vibration within the carbon frameworks of GO. The FTIR spectrum of $CoFe_2O_4$/GO hybrids represents several

differences from that of GO. The peaks at 2926 and 2856 cm^{-1} are associated with the asymmetric and symmetric stretching vibration of $-CH_2$, respectively. The peak of the C=O vibration shifts to lower wavenumbers of 1605 cm^{-1}, indicating the formation of COOM (M=Fe, Co).[55] The peaks at 595 and 415 cm^{-1} are assigned to the stretching vibration of Fe (Co)-O in the tetrahedral and octahedral sites of the spinel ferrite.[23] These results suggest that $CoFe_2O_4$ nanocrystals were linked to the surface of GO by covalent bonding. However, the FTIR spectrum of FeCo/GNs hybrids does not exhibit any peak associated with above-mentioned the oxygen-containing functional groups. The mossy bands in the range of 1300-2000 cm^{-1} can be attributed to the skeletal vibration of the graphene nanosheets.[82] The additional peak at 669 cm^{-1} is probably due to FeCo nanocrystals. These results indicated that the oxygen-containing functional groups were completely removed after the annealing treatment and thus GO was effectively reduced into GNs in the FeCo/GNs hybrids.

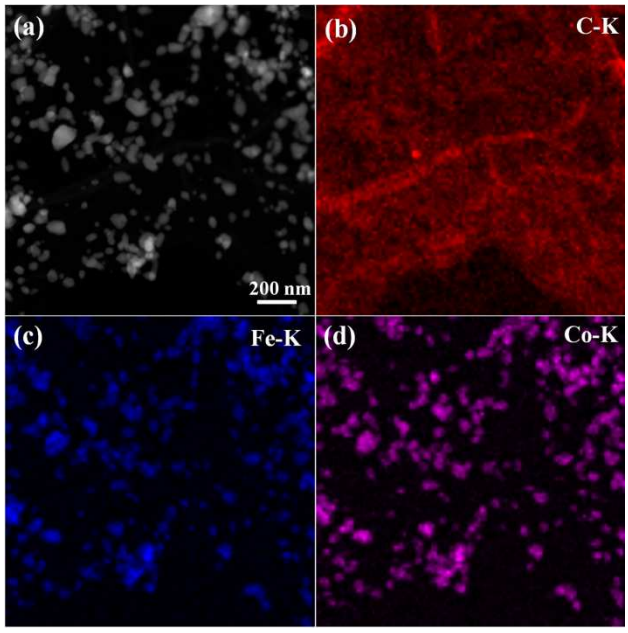

Fig. 7 Element mapping of FeCo/GNs hybrids: (a) Representative HAADF-STEM image of FeCo/GNs hybrids; (b) carbon mapping; (c) iron mapping; (d) cobalt mapping.

To further determine the situation of FeCo nanocrystals supported on graphene, HAADF-STEM image and EDX elemental mapping techniques were used to investigate the morphology and chemical element distributions of FeCo/GNs hybrids. HAADF-STEM image, called *Z*-contrast image (*Z* is the atomic number), is ideal and powerful for the characterization of heterogeneous hybrids with components of different atomic numbers.[83] It is believed that this *Z*-contrast images could offer a better distinction between FeCo (average $Z \approx 26.5$) and C ($Z = 6$). Fig. 7 shows the HAADF-STEM image for the FeCo/GNs hybrids, as well as the corresponding EDX elemental mapping of C (K_α, 0.28 keV), Fe (K_α, 6.4 keV) and Co (K_α, 6.9 keV). In the HAADF-STEM image (Fig. 7 (a)), the FeCo nanocrystals present bright dots that decorate on the surface of GNs with relative grey color. Each individual FeCo nanocrystals reveal a uniform contrast, indicating that the FeCo nanocrystals have a pure chemical phase. The EDX element mapping of C (Fig. 7 (b)) shows a uniform distribution throughout the whole GNs, while the Fe (Fig. 7 (c)) and Co (Fig. 7 (d)) coexist in the exact positions where FeCo nanocrystals located in Fig. 7 (a). These results are in well agreement with the above TEM observations.

The magnetic measurements of $CoFe_2O_4$/GO and FeCo/GNs hybrids were conducted by VSM at room temperature. The hysteresis loops for both samples are shown in Fig. 8. The $CoFe_2O_4$/GO hybrids exhibit superparamagnetic properties at room temperature in which the anisotropy energy barrier of a single $CoFe_2O_4$ particle can succumb to thermal energy. The saturation magnetization (M_s) of $CoFe_2O_4$/GO is about 53 emu/g that is comparable to freestanding $CoFe_2O_4$ nanocrystals with similar size,[84] confirming that there is no aggregated crystals formed. This small M_s in respect to bulk counterpart (74 emu/g) may be ascribed to the weight-fraction of GO as well as the possible effect of surface spin canting on the $CoFe_2O_4$ nanocrystals.[84] After thermal reduction, FeCo/GNs hybrids shows ferromagnetic behavior with a M_s as high as 187 emu/g. The enhancement of M_s for FeCo/GNs hybrids is mainly attributed to the large particle size and magnetic moment of FeCo. In addition, the thermal treatment process may increase the crystallinity and reduce the defect of the sample, which can also lead to the enhancement of M_s. The low coercivity of the FeCo/GNs hybrids (H_c = 400 Oe) indicate its nature of soft magnetic materials.

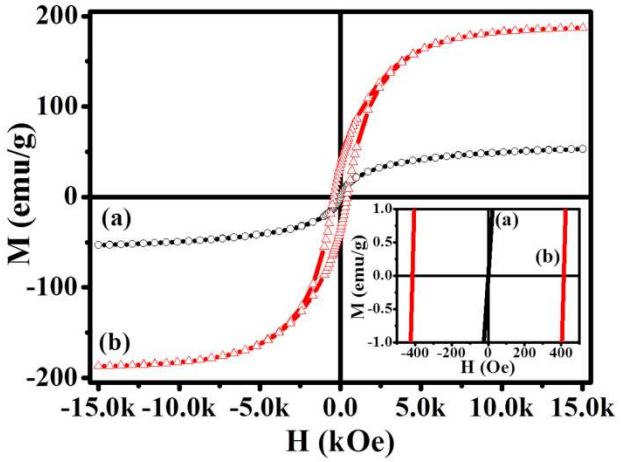

Fig. 8 Magnetic hysteresis loops of (a) $CoFe_2O_4$/GO and (b) FeCo/GNs hybrids at 300 K.

Since the microwave absorption properties of a material is determined by their complex permeability ($\mu_r = \mu' - j\mu''$) and permittivity ($\varepsilon_r = \varepsilon' - j\varepsilon''$), the frequency dependence of complex permeability and permittivity for the $CoFe_2O_4$/GO and FeCo/GNs hybrids are measured using a network analyzer and shown in Fig. 9. The pristine $CoFe_2O_4$ nanocrystals with the same size are used as control. In whole measurement, the samples were dispersed in a flexible paraffin matrix with concentration of 50 wt%. Fig. 9 (a-c) shows the frequency dependence of complex permeability for the samples. For the pure $CoFe_2O_4$ nanocrystals (Fig. 9 (a)) and $CoFe_2O_4$/GO hybrids (Fig. 9 (b)), the real part of complex permeability (μ') decreases from about 1.4 to 1.0 with the increase of frequency from 0.1 to 18 GHz, whereas the imaginary part of complex permeability (μ'') is almost constant over the whole frequency range with a slightly fluctuation ($\mu'' \approx 0.05$).

The decreased permeability of magnetic materials are frequently observed when they were coated or embedded by nonmagnetic material, which can be attributed to the reduction of saturation

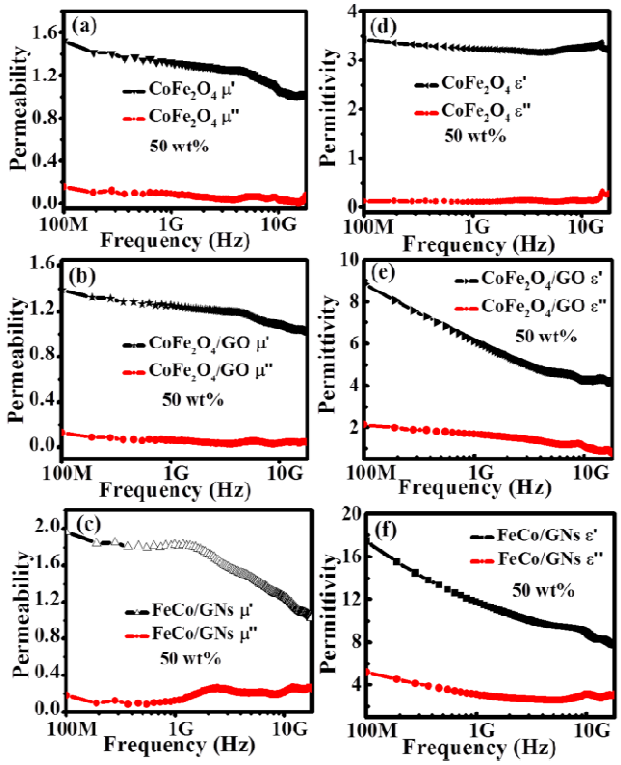

Fig. 9 Frequency dependence of complex permeability for the paraffin-based composites (50 wt%): (a) pure $CoFe_2O_4$ nanocrystals, (b) $CoFe_2O_4$/GO hybrids and (c) FeCo/GNs hybrids; Frequency dependence of complex permittivity for the paraffin-based composites (50 wt%): (d) pure $CoFe_2O_4$ nanocrystals, (e) $CoFe_2O_4$/GO hybrids and (f) FeCo/GNs hybrids.

magnetization after combination with nonmagnetic materials. However, the variation of the permeability between the pure $CoFe_2O_4$ and $CoFe_2O_4$/GO hybrids prepared in this work is quite small, indicating that the effect of additional GO in hybrids on the complex permeability can be negligible. This counterintuitive result is possibly attributed to the low weighted-fraction of nonmagnetic GO and well-dispersed $CoFe_2O_4$ nanocrystalls on the GO that weakens the interparticle interactions.[17] The μ' value for FeCo/GNs hybrids (Fig. 9 (c)) is about 1.8 in the range of 0.1-1.5 GHz and then declines rapidly to 1.0 at 18 GHz. In comparison with the pure $CoFe_2O_4$ nanocrystals and $CoFe_2O_4$/GO hybrids, the enhancement of μ' for FeCo/GNs hybrids is obviously due to its lager saturation magnetization. The μ'' curve for FeCo/GNs hybrids presents a higher value, which varied from 0.08 to 0.26. In addition, two ferromagnetic resonance bands located at around 2.4 and 12.2 GHz can be seen on the μ'' curve. These ferromagnetic resonances are believed to cause magnetic loss, which is promised to a significant enhancement of the microwave absorption for FeCo/GNs hybrids. The frequency dependence of complex permittivity for the three samples is shown in Fig. 9 (d-f). The real part (ε') and imaginary part (ε'') of complex permittivity for the pure $CoFe_2O_4$ nanocrystals (Fig. 9 (d)) are nearly constant over the 0.1-18 GHz range with an inconspicuous undulation ($\varepsilon' \approx 3.2$ and $\varepsilon'' \approx 0.15$). For $CoFe_2O_4$/GO hybrids (Fig. 9 (e)), the measured complex permittivity show a significant change. The values of ε' and ε'' declines from 8.85 to 4.2 and 2.14 to 0.75, respectively, 2.7 and 14 times larger than that of pure $CoFe_2O_4$ nanocrystals at 0.1 GHz. This should be ascribed to the increased electric polarization and electrical conductivity in presence of GO. By contrast, the FeCo/GNs hybrids (Fig. 9 (f)) exhibited much higher values of complex permittivity, in which ε' decreases from 17.45 to 7.7 and ε'' varies between 5.22 and 2.54, 5.5 and 35 times than that of $CoFe_2O_4$ nanocrystals at 0.1 GHz. The superior complex permittivity for FeCo/GNs hybrids is attributed to high conductivity of the combination of metallic FeCo alloys and GNs. Similarly, this significant increase of complex permittivity is

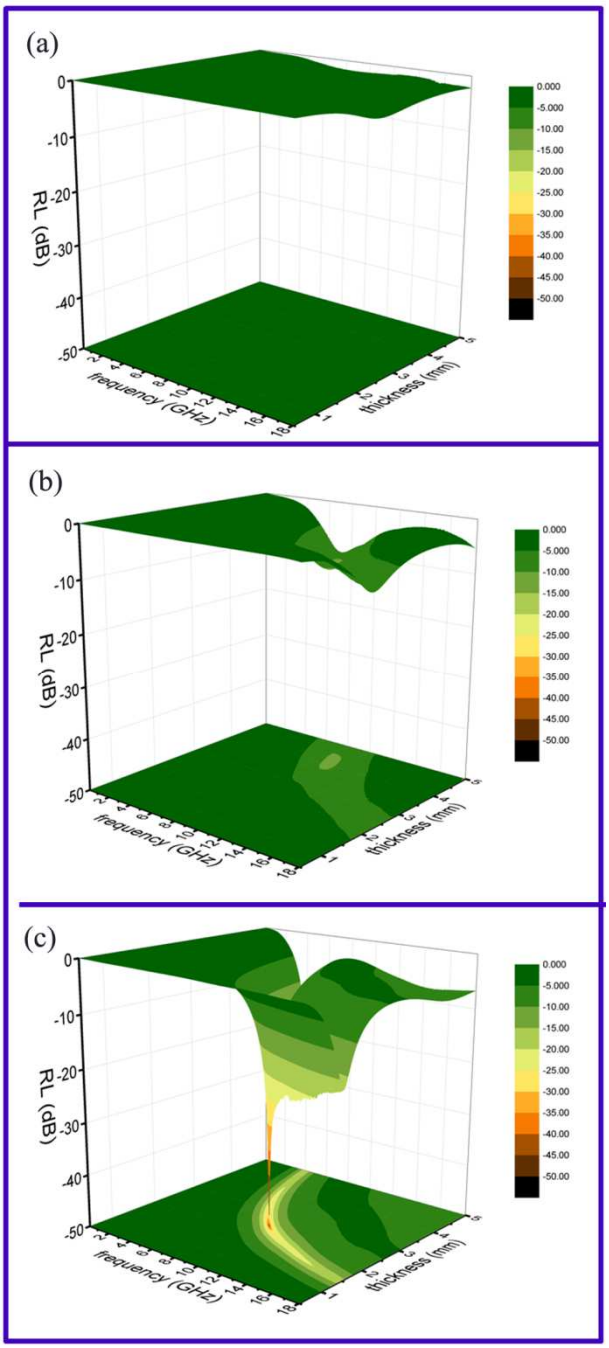

Fig. 10 Three-dimensional representation of RL values for the paraffin-based composites (50 wt%): (a) pure $CoFe_2O_4$ nanocrystals, (b)

$CoFe_2O_4$/GO hybrids and (c) FeCo/GNs hybrids.

expected to be an important contribution for the enhancement of the microwave absorption of FeCo/GNs hybrids. Moreover, the frequency dependence of dissipation factors represented by the magnetic loss tangent ($\tan\delta_\mu = \mu''/\mu'$) and dielectric loss tangent ($\tan\delta_\varepsilon = \varepsilon''/\varepsilon'$) for the three samples were displayed in Fig. S3. The values of $\tan\delta_\mu$ and $\tan\delta_\varepsilon$ for FeCo/GNs hybrids are obviously improved, which indicate that combination of the FeCo nanocrystals with high saturation magnetization and lightweight graphene are significant for the enhancement of both magnetic loss and dielectric loss.

The conductivities for the $CoFe_2O_4$/GO and FeCo/GNs hybrids are measured by four-point probe technique, which are 8.28×10^{-4} and 2.93 S m^{-1}, respectively. And the skin depth with the frequency at 1 GHz for the two hybrids are about 0.5 and 7 $\times10^{-3}$ m, respectively (The U-I curves for the two samples and the detail calculated process can be seen in Fig. S4 and S5, supporting information).

In view of the novel nanostructure and remarkable complex permeability and permittivity properties of the FeCo/GNs hybrids, the microwave absorption behaviors of the sample are investigated. The physical model for the interaction of microwave and FeCo/GNs hybrids is shown in Fig. 1. When the microwave is incident on the absorber backed by a metal plate, the incident microwave is partially consumed by the absorber through microwave loss mechanisms, partially reflected from the front interface of the absorber layer (air-absorber interface), and partially reflected from the back interface of the absorber layer (absorber-metal interface). The dominant loss of the incident microwave is absorption mechanism, in which the energy consumption is owing to the magnetic and dielectric loss. The magnetic loss is attributed to the natural resonance loss of the magnetic FeCo nanocrystals. The dielectric loss is due to the 2D graphene nanosheets with large surface area and high aspect ratio, which can constitute a network for dispersing charges. Besides, the magnetic and dielectric loss of microwave convert into heat, which will spread rapidly to the environment owing to the remarkale thermal conductivity of graphene. When the microwave absorption properties is strong enough, the reflected microwave is weak and cannot be detected by the radar. Typically, the RL value is used to evaluate the microwave absorption efficiency of materials, for example, the RL value of -10 dB is comparable to 90% of microwave absorption. The RL curves of an absorber backed by a metal plate were calculated according to the transmit line theory, which is based on the measured complex permeability and permittivity at a given absorber thickness and frequency by the following equation:[2, 66]

$$RL = 20\log\left|\frac{Z_{in}-Z_0}{Z_{in}+Z_0}\right| \quad (1)$$

$$Z_{in} = Z_0\left(\frac{\mu_r}{\varepsilon_r}\right)^{1/2}\tanh\left\{j\left(\frac{2\pi fd}{c}\right)(\mu_r\varepsilon_r)^{1/2}\right\} \quad (2)$$

where Z_{in} is the input impendence of absorber, Z_0 is the impedance of air, f is the frequency of electromagnetic wave, d is the thickness of a microwave absorber and c is the velocity of light in vacuum. Fig. 10 shows the variations of the RL values versus frequency for the three samples at different thicknesses. It is clear that the absorption peaks for the three samples shift toward low frequency region as the absorber thickness increases. The RL values for the pure $CoFe_2O_4$ nanocrystals (Fig. 10 (a)) cannot reach -10 dB within the thickness range of 1.0-6.0 mm, indicating that the $CoFe_2O_4$ nanocrystals could not be used for the practical applications. For the $CoFe_2O_4$/GO hybrids (Fig. 10 (b)), the RL values exceeding -10 dB are reached in the 8.1-9.8 GHz with absorber thicknesses of 4.0-4.5 mm, and a minimum RL of -10.8 dB is obtained at 9.2 GHz with a thickness of 4.0 mm. For the FeCo/GNs hybrids (Fig. 10 (c)), the RL values less than -10 dB are found in the wide frequency range of 3.4-18 GHz with the thicknesses of 1.5-6.0 mm, while an optimal RL of -40.2 dB is achieved at 8.9 GHz when the matching thickness of 2.5 mm. The results suggest that the FeCo/GNs hybrids have remarkable absorbing characteristic in wide frequency bands from C to K_u band (4-18 GHz), especially covering the entire X band (8-12 GHz) which is of great interest for the military radar and direct broadcast satellite (DBS) due to its high resolution imaging and precision target identification.[23] When the thickness of the absorber is as thin as 1.5 mm, the microwave absorption band of FeCo/GNs hybrids exceeds 18 GHz that is over the measurement frequency range, indicating that the FeCo/GNs hybrids can also be used at K band for further applications. This is probably due to the addition of a finite thickness of these microwave-absorbing materials, in which a broad band of light absorbed by graphene was consumed by the addition of $CoFe_2O_4$ and FeCo nanocrystals.

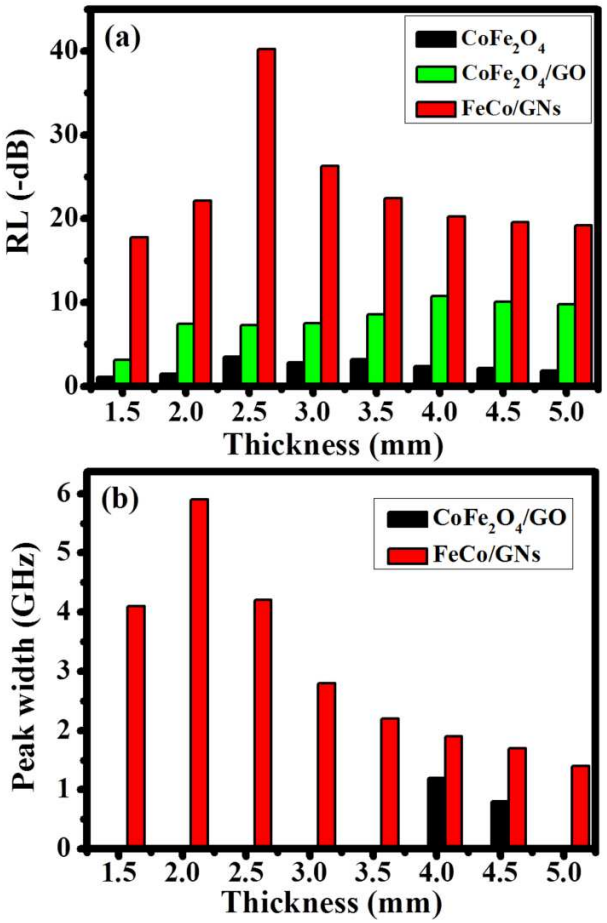

Fig. 11 Comparison of the (a) RL values and (b) peak width (RL > -10

dB) of the three samples at different thicknesses.

Fig. 11 (a) shows the comparison of the minimum RL values at different matching thicknesses for the samples. The FeCo/GNs hybrids exhibit remarkable microwave absorption properties at every thickness as compared to the other two samples. Fig. 11 (b) presents the bandwidth (Δf) of the FeCo/GNs hybrids at -10 dB. The bandwidth becomes narrower as the matching thickness increases. The broad bandwidth indicates that the FeCo/GNs hybrids can be used in a wide frequency range. All the results above suggest that the FeCo/GNs hybrids are the most promising candidate for enhanced microwave absorber among these samples.

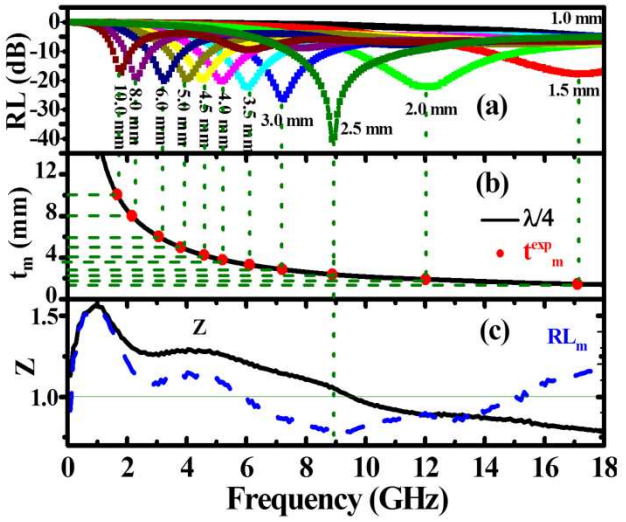

Fig. 12 (a) Frequency dependence of RL values for FeCo/GNs hybrids (50 wt%) with twelve thicknesses; (b) simulations of the absorber thickness (t_m) versus peak frequency (f_m) for FeCo/GNs hybrids (50 wt%) under λ/4 condition; (c) the modulus of normalized input impedance ($|Z_{in}/Z_0|$) for FeCo/GNs hybrids (50 wt%).

To understand the physical phenomenon and possible mechanism giving rise to the enhanced microwave absorption properties of FeCo/GNs hybrids, the quarter-wavelength matching model was used to analyze the experimental results, in which the relationship between the absorber thickness (t_m) and the peak frequency (f_m) can be described by the following equation:[23]

$$t_m = \frac{nc}{4f_m\sqrt{|\mu_r||\varepsilon_r|}} \quad (3)$$

where $|\mu_r|$ and $|\varepsilon_r|$ are respectively the modulus of the measured μ_r and ε_r at f_m, and c is the velocity of light in a vacuum. According to the quarter-wavelength matching model, when the matching thickness of the FeCo/GNs hybrids/paraffin composites satisfies the equation (3), the emerging microwave reflected from the air-absorber interface and the absorber-metal interface are out of phase by 180 °, resulting in an extinction of each other at the air-absorber interface. Fig. 12 (a) shows the variations of the RL curves versus frequency of the FeCo/GNs hybrids/paraffin composites with twelve thicknesses. Based on the quarter wavelength (λ/4) condition, a simulation of the absorber thickness (t_m) versus peak frequency (f_m) for the FeCo/GNs hybrids/paraffin composites is presented in Fig. 12 (b). The red dots on the λ/4 curve are the matching thicknesses (denoted as t_m^{exp}) versus frequency of the absorption peaks, which were directly obtained from the curves in Fig. 12 (a). It is clear that the relationship between the experimental matching thickness (t_m^{exp}) and peak frequency is in good agreement with the simulations using the quarter wavelength (λ/4) principle for FeCo/GNs hybrids. The frequency dependence of $Z = |Z_{in}/Z_0|$ for FeCo/GNs hybrids (black dashed curve) is obtained by the equation (2) as displayed in Fig. 12 (c), in which the relationship between frequency and RL at the matching thickness (RL_{rm}) is shown by the blue solid curve. When the matching frequency is 8.9 GHz, the minimum RL can be obtained (the blue solid curve in Fig. 12 (c)) and the relevant Z is close to 1 (the black dashed curve in Fig. 12 (c)), while the matching thickness is 2.5 mm on the λ/4 curve (Fig. 12 (b)). The results indicate that the the relationship between matching thickness and frequency for the microwave absorption of FeCo/GNs hybrids can be well-explained by the quarter-wave theory. Moreover, the quarter-wave principle is an efficient tool to provide a significant guide for the thickness design required for the microwave absorber, when the complex permittivity and permeability of the corresponding microwave absorption materials are measured.

Conclusions

In summary, we have successfully fabricated $CoFe_2O_4$/GO hybrids by a facile one-pot polyol route. These $CoFe_2O_4$/GO hybrids could be further converted into FeCo/GNs hybrids through H_2/NH_3-annealing treatment, in which graphene oxide was reduced into graphene along with the formation of FeCo alloy nanocrystals. The obtained $CoFe_2O_4$/GO and FeCo/GNs hybrids shows a unique sandwich structure where single crystal $CoFe_2O_4$ and FeCo nanocrystals are evenly distributed on both side of GO and GN without any aggregation. Experimental data indicate that both $CoFe_2O_4$/GO and FeCo/GNs hybrids show the improved microwave absorption properties, which is ascribed to the synergistic effect of magnetic nanoparticle and graphene. In particular, FeCo/GNs hybrids exhibited significantly enhancement in both complex permeability and permittivity with respect to $CoFe_2O_4$ and $CoFe_2O_4$/GO due to remarkable complex permeability from FeCo nanocrystals and permittivity from graphene. In addition, the metallic nature of FeCo alloy may also contribute to the improved permittivity of FeCo/GNs hybrids. As a result, the FeCo/GNs hybrids exhibited a minimum RL value of -40.2 dB at 8.9 GHz with a matching thickness of 2.5 mm and a broad bandwidth (RL ≤ -10 dB) in 3.4-18 GHz range for the thicknesses of 1.5-6.0 mm. The comprehensive performance of light-weight FeCo/GNs hybrids absorber is among the best of reported to date. Moreover, it is found that the enhanced microwave-absorbing behavior of FeCo/GNs hybrids could be well explained by the quarter-wavelength matching model, facilitating the design of FeCo/GNs hybrids film for practical application. The results suggest that the FeCo/GNs hybrids can serve as ideal candidate for the manufacture of light-weight and high-efficiency microwave-absorbing devices. In addition, the facile synthesis of high-quality sandwich-structured $CoFe_2O_4$/GO and FeCo/GNs hybrids presented in this work also open the opportunities to fabricate other functional nanoparticle/grephene hybrid systems for various industrial application such as energy conversion, lithium ion batteries, catalysis and electromagnetic

shielding materials.

Acknowledgements

This work was supported by the grants from the National Natural Science Foundation of China (J1210055, J1310016, 11274145, 21371140 and 21376192), the Natural Science Foundation of Shannxi Province,China (2014JQ1040), the Foundation of Educational department of Shaanxi Province, China (14JK1727), the Science Foundation of Northwest University (13NW13), the Basic Scientific Research Business Expenses of the Central University, Open Project of Key Laboratory for Magnetism and Magnetic Materials of the Ministry of Education from Lanzhou University and the open projects from Institute of Photonics and Photo-Technology of Northwest University (China).

Notes and references

[a] *Department of Physics, Northwest University, Xi'an, 710069, China; E-mail: fanhm@nwu.edu.cn*
[b] *School of Physical Science and Technology, Lanzhou University, Lanzhou, 730000, China; E-mail: pengy@lzu.edu.cn*
[c] *Center for Applied Chemistry, Frontier Institute of Science and Technology, Xi'an Jiaotong University, Xi'an 710069, China*
[d] *Shaanxi Key Laboratory of Degradable Biomedical Materials, School of Chemical Engineering, Northwest University, Xi'an, 710069, China*
[e] *State Key Laboratory of Applied Organic Chemistry, College of Chemistry and Chemical Engineering, Lanzhou University, Lanzhou 730000, China*
[§] *Xinghua Li and Juan Feng contributed equally to this work.*
† Electronic Supplementary Information (ESI) available: [*It contains EDX patterns, AFM image and loss tangent spectra.*]. See DOI: 10.1039/b000000x/

1 J. W. Liu, R. C. Che, H. J. Chen, F. Zhang, F. Xia, Q. S. Wu and M. Wang, *Small*, 2012, **8**, 1214.
2 T. Xia, C. Zhang, N. A. Oyler and X. B. Chen, *Adv. Mater.,* 2013, **25**, 6905.
3 J. L Guo, X. L. Wang, P. L. Miao, X. P. Liao, W. H. Zhang and B. Shi, *J. Mater. Chem.,* 2012, **22**, 11933.
4 G. B. Sun, B. X. Dong, M. H. Cao, B. Q. Wei and C. W. Hu, *Chem. Mater.,* 2011, **23**, 1587.
5 C. L. Zhu, M. L. Zhang, Y. J. Qiao, G. Xiao, F. Zhang and Y. J. Chen, *J. Phys. Chem. C,* 2010, **114**, 16229.
6 W. M. Zhu, L. Wang, R. Zhao, J. W. Ren, G. Z. Lu and Y. Q. Wang, *Nanoscale,* 2011, **3**, 2860.
7 X. A. Fan, J. G. Guan, Z. Z. Li, F. Z. Mou, G. X. Tong and W. Wang, *J. Mater. Chem.,* 2010, **20**, 1676.
8 C. Z. He, S. Qiu, X. Z. Wang, J. R. Liu, L. Q. Luan, W. Liu, M. Itoh and K. I. Machida, *J. Mater. Chem.,* 2012, **22**, 22160.
9 G. X. Tong, Q. Hu, W. H. Wu, W. Li, H. S. Qian and Y. Liang, *J. Mater. Chem.,* 2012, **22**, 17494.
10 R. B. Wu, K. Zhou, Z. H. Yang, X. K. Qian, J. Wei, L. Liu, Y. Z. Huang, L. B. Kong and L. Y. Wang, *CrystEngComm.,* 2013, **15**, 570.
11 F. Xia, J. W. Liu, D. Gu, P. F. Zhao, J. Zhang and R. C. Che, *Nanoscale,* 2011, **3**, 3860.
12 M. Zhou, X. Zhang, J. M. Wei, S. L. Zhao, L. Wang and B. X. Feng, *J. Phys. Chem. C,* 2011, **115**, 1398.
13 S. He, G. S. Wang, C. Lu, J. Liu, B. Wen, H. Liu, L. Guo and M. S. Cao, *J. Mater. Chem. A,* 2013, **1**, 4685.
14 A. Mdarhri, C. Brosseau, M. Zaghrioui and I. E. Aboudi, *J. Appl. Phys.,* 2012, **112**, 034118.
15 F. Qin and C. Brosseau, *J. Appl. Phys.,* 2012, **111**, 061301.
16 X. Bai, Y. H. Zhai and Y. Zhang, *J. Phys. Chem. C,* 2011, **115**, 11673.
17 N. Li, M. H. Cao and C. W. Hu, *J. Mater. Chem.,* 2012, **22**, 18426.
18 J. H. Zhu, S. Y. Wei, N. Haldolaarachchige, D. P. Youg and Z. H. Guo, *J. Phys. Chem. C,* 2011, **115**, 15304.
19 H. Guo, Y. Q. Zhan, Z. R. Chen, F. B. Meng, J. J. Wei and X. B. Liu, *J. Mater. Chem. A,* 2013, **1**, 2286.
20 X. L. Dong, X. F. Zhang, H. Huang and F. Zuo, *Appl. Phys. Lett.* 2008, **92**, 013127.
21 X. G. Liu, D. Y. Geng, H. Meng, P. J. Shang and Z. D. Zhang, *Appl. Phys. Lett.,* 2008, **92**, 173117.
22 J. Q. Wei, J. B. Wang, Q. F. Liu, L. Qiao, T. Wang and F. S. Li, *J. Phys. D: Appl. Phys.,* 2010, **43**, 115001.
23 X. H. Li, H. B. Yi, J. W. Zhang, J. Feng, F. S. Li, D. S. Xue, H. L. Zhang, Y. Peng and N. J. Mellors, *J. Nanopart. Res.,* 2013, **15**, 1472.
24 H. Wang, H. H. Guo, Y. Y. Dai, D. Y. Geng, Z. Han, D. Li, T. Yang, S. Ma, W. Liu and Z. D. Zhang, *Appl. Phys. Lett.,* 2012, **101**, 083116.
25 N. Li, C. W. Hu and M. H. Cao, *Phys. Chem. Chem. Phys.,* 2013, **15**, 7685.
26 X. G. Liu, Z. Q. Ou, D. Y. Geng, Z. Han, J. J. Jiang, W. Liu and Z. D. Zhang, *Carbon* 2010, **48**, 891.
27 X. G. Liu, B. Li, D. Y. Geng, W. B. Cui, F. Yang, Z. G. Xie, D. J. Kang and Z. D. Zhang, *Carbon,* 2009, **47**, 470.
28 X. S. Qi, Y. Yang, W. Zhong, C. Qin, Y. Deng, C. Au and Y. W. Du, *Carbon,* 2010, **48**, 3512.
29 R. T. Lv, F. Y. Kang, J. L. Gu, X. C. Gui, J. Q. Wei, K. L. Wang and D. H. Wu, *Appl. Phys. Lett.,* 2008, **93**, 223105.
30 F. S. Wen, F. Zhang and Z. Y. Liu, *J. Phys. Chem. C,* 2011, **115**, 14025.
31 R. C. Che, L. M. Peng, X. F. Duan, Q. Chen and X. L. Liang, *Adv. Mater.,* 2004, **16**, 401.
32 R. T. Lv, A. Y. Cao, F. Y. Kang, W. X. Wang, J. Q. Wei, J. L. Gu, K. L. Wang and D. H. Wu, *J. Phys. Chem. C,* 2007, **111**, 11475.
33 Z. J. Wang, L. N. Wu, J. G. Zhou, W. Cai, B. Z. Shen and Z. H. Jiang, *J. Phys. Chem. C,* 2013, **117**, 5446.
34 C. N. R. Rao, A. K. Sood, K. S. Subrahmanyam and A. Govindaraj, *Angew. Chem. Int. Ed.,* 2009, **48**, 7752.
35 Y. W. Zhu, S. Murali, W. W. Cai, X. S. Li, J. W. Suk, J. R. Potts and R. S. Ruoff, *Adv. Mater.,* 2010, **22**, 3906.
36 X. Huang, Z. Y. Zeng, Z. X. Fan, J. Q. Liu and H. Zhang, *Adv. Mater.,* 2012, **24**, 5979.
37 W. G. Xu, X. Ling, J. Q. Xiao, M. S. Dresselhaus, J. Kong, H. X. Xu, Z. F. Liu and J. Zhang, *Proc. Natl. Acad. Sci. USA,* 2012, **109**, 9281.
38 V. Georgakilas, M. Otyepka, A. B. Bourlinos, V. Chandra, N. Kim, K. C. Kemp, P. Hobza, R. Zboril and K. S. Kim, *Chem. Rev.,* 2012, **112**, 6156.
39 X. J. Wan, G. K. Long, L. Huang and Y. S. Chen, *Adv. Mater.*, 2011, **23**, 5342.
40 R. S. Edward and K. S. Coleman, *Nanoscale,* 2013, **5**, 38.
41 S. X. Wu, Q. Y. He, C. L. Tan, Y. D. Wang and H. Zhang, *Small,* 2013, **9**, 1160.
42 L. P. Biró, P. N. Incze and P. Lambin, *Nanoscale,* 2012, **4**, 1824.
43 T. Kuila, S. Bose, A. K. Mishra, P. Khanra, N. H. Kim and J. H. Lee, *Prog. Mater. Sci.,* 2012, **57**, 1061.
44 C. Wang, X. J. Han, P. Xu, X. L. Zhang, Y. C. Du, S. R. Hu, J. Y. Wang and X. H. Wang, *Appl. Phys. Lett.,* 2011, **98**, 072906.
45 J. J. Liang, Y. Wang, Y. Huang, Y. F. Ma, Z. F. Liu, J. M. Cai, C. D. Zhang, H. J. Gao and Y. S. Chen, *Carbon,* 2009, **47**, 922.
46 D. X. Yan, P. G. Ren, H. Pang, Q. Fu, M. B. Yang and Z. M. Li, *J. Mater. Chem.,* 2012, **22**, 18772.
47 W. L. Song, M. S. Cao, M. M. Lu, J. Yang, H. F. Ju, Z. L. Hou, J. Liu, J. Yuan and L. Z. Fan, *Nanotech.,* 2013, **24**, 115708.
48 H. L. Yu, T. S. Wang, B. Wen, M. M. Lu, Z. Xu, C. L. Zhu, Y. J. Chen, X. Y. Xue, C. W. Sun and M. S. Cao, *J. Mater. Chem.,* 2012, **22**, 21679.
49 Q. J. Xiang, J. G. Yu and M. Jaroniec, *Chem. Soc. Rev.,* 2012, **41**, 782.
50 X. Huang, Z. Y. Yin, S. X. Wu, X. Y. Qi, Q. Y. He, Q. C. Zhang, Q. Y. Yan, F. Boey and H. Zhang, *Small,* 2011, **7**, 1876.
51 Y. Huang, J. J. Liang and Y. S. Chen, *Small,* 2012, **8**, 1805.

52 X. Huang, X. Y. Qi, F. Boey and H. Zhang, *Chem. Soc. Rev.,* 2012, **41**, 666.
53 S. Bai and X. P. Shen, *RSC Adv.,* 2012, **2**, 64.
54 C. Xu, X. Wang and J. W. Zhu, *J. Phys. Chem. C,* 2008, **112**, 19841.
55 X. Y. Yang, X. Y. Zhang, Y. F. Ma, Y. Huang, Y. S. Wang and Y. S. Chen, *J. Mater. Chem.,* 2009, **19**, 2710.
56 X. X. Ma, H. Q. Tao, K. Yang, L. Z. Feng, L. Cheng, X. Z. Shi, Y. G. Li, L. Guo and Z. Liu, *Nano Res.,* 2012, **5**, 199.
57 F. Tuinstra and J. L. Koenig, *J. Chem. Phys.,* 2003, **53**, 1128.
58 Y. J. Chen, Q. S. Wang, C. L. Zhu, P. Gao, Q. Y. Qoyang, T. S. Wang, Y. Ma and C. W. Sun, *J. Mater. Chem.,* 2012, **22**, 5924.
59 H. Jabeen, V. Chandra, S. Jung, J. W. Lee, K. S. Kim and S. B. Kim, *Nanoscale,* 2011, **3**, 3583.
60 B. J. Li, H. Q. Cao, J. Shao, M. Z. Qu and J. H. Warner, *J. Mater. Chem.,* 2011, **21**, 5069.
61 Q. T. Qu, S. B. Yang and X. L. Feng, *Adv. Mater.,* 2011, **23**, 5574.
62 S. Mandal and S. K. Saha, *Nanoscale,* 2012, **4**, 986.
63 K. Singh, A. Ohlan, V. H. Pham, R. Balasubramaniyan, S. Varshney, J. Jang, S. H. Hur, W. M. Choi, M. Kumar, S. K. Dhawan, B. S. Kong and J. S. Chung, *Nanoscale,* 2013, **5**, 2411.
64 X. Sun, J. P. He, G. X. Li, J. Tang, T. Wang, Y. X. Guo and H. R. Xue, *J. Mater. Chem. C,* 2013, **1**, 765.
65 A. P. Singh, P. Garg, F. Alam, K. Singh, R. B. Mathur, R. P. Tandon, A. Chandra and S. K. Dhawan, *Carbon,* 2012, **50**, 3868.
66 D. Z. Chen, G. S. Wang, S. He, J. Liu, L. Guo and M. S. Cao, *J. Mater. Chem. A,* 2013, **1**, 5996.
67 M. Fu, Q. Z. Jiao and Y. Zhao, *J. Mater. Chem. A,* 2013, **1**, 5577.
68 T. T. Chen, F. Deng, J. Zhu, C. F. Chen, G. B. Sun, S. L. Ma and X. J. Yang, *J. Mater. Chem.,* 2012, **22**, 15190.
69 Y. Cao, Q. M. Su, R. C. Che, G. H. Du and B. S. Xu, *Synthetic Mat.,* 2012, **162**, 968.
70 C. G. Hu, Z. Y. Mou, G. W. Lu, N. Chen, Z. L. Dong, M. J. Hu and L. T. Qu, *Phys. Chem. Chem. Phys*., 2013, **15**, 13038.
71 P. B. Liu and Y. Huang, *RSC Adv.,* 2013, **3**, 19033.
72 J. K. Liu, H. Q. Cao, J. P. Xiong and Z. Y. Cheng, *CrystEngComm.,* 2012, **14**, 5140.
73 M. Zhang, D. N. Lei, X. M. Yin, L. B. Chen, Q. H. Li, Y. G. Wang and T. H. Wang, *J. Mater. Chem.,* 2010, **20**, 5538.
74 J. Z. Wang, C. Zhong, D. Wexler, N. H. Idris, Z. X. Wang, L. Q. Chen and H. K. Liu, *Chem. Eur. J.,* 2011, **17**, 661.
75 K. Y. Chen, C. Xiang, L. C. Li, H. S. Qian, Q. S. Xiao and F. Xu, *J. Mater. Chem.,* 2012, **22**, 6449.
76 Y. Zhang, B. Chen, L. M. Zhang, J. Huang, F. H. Chen, Z. P. Yang, J. L. Yao and Z. J. Zhang, *Nanoscale,* 2011, **3**, 1446.
77 X. W. Wei, G. X. Zhu, Y. J. Liu, Y. H. Ni, Y. Song and Z. Xu, *Chem. Mater.,* 2008, **20**, 6248.
78 J. J. Jiang, D. Li, D. Y. Geng, J. An, J. He, W. Liu and Z. D. Zhang, *Nanoscale,* 2014, **6**, 3967.
79 A. M. Nicolson, G. F. Ross, *IEEE Trans. Instrum. Meas.*, 1970, **19**, 377.
80 J. C. Meyer, A. K. Geim, M. I. Katsnelson, K. S. Novoselov, D. Obergfell, S. Roth, C. Girit and A. Zettl, *Solid State Commun.,* 2007, **143**, 101.
81 C. Mattevi, Eda G, Agnoli S, et al. *Adv. Funct. Mater.* 2009, **19**, 2577.
82 C. Nethravathi and M. Rajamathi, *Carbon* 2008, **46**, 1994.
83 J. C. González, J. C. Hernández, M. López-Haro, E. del Río, J. J. Delgado, A. B. Hungría, S. Trasobares, S. Bernal, P. A. Midgley and J. J. Calvino, *Angew. Chem. Int. Ed.,* 2009, **48**, 5313.
84 X. H. Li, C. L. Xu, X. H. Han, L. Qiao, T. Wang and F. S. Li, *Nanoscale Res. Lett.,* 2010, **5**, 1039.